Wavy Graphene-Like Network Forming During Pyrolysis of Polyacrylonitrile into Carbon Fiber

Toru Ishikawa,[1] Fumihiko Tanaka,[1,2,*] Kosuke Kurushima,[3] Akira Yasuhara,[4] Ryusuke Sagawa,[4] Tatsuya Fujita,[5] Ryohei Yonesaki,[5] Katsuhiko Iseki,[6] Takayuki Nakamuro,[7] Koji Harano,[7,8,*] and Eiichi Nakamura[7,*]

[1] Composite Materials Research Laboratories, Toray Industries, Inc., 1515 Tsutsui, Masaki-cho, Iyo-gun, Ehime, 791-3193, Japan

[2] Torayca Technical Department, Toray Industries, Inc., 1515 Tsutsui, Masaki-cho, Iyo-gun, Ehime, 791-3193, Japan

[3] Toray Research Center, 3-3-7 Sonoyama, Otsu, Shiga, 520-8567, Japan

[4] JEOL Ltd., 3-1-2 Musashino, Akishima, Tokyo, 196-8558, Japan

[5] Pharmaceutical Research Laboratories, Toray Industries, Inc., 6-10-1 Tebiro, Kamakura, Kanagawa, 248-8555, Japan

[6] Technology Center, Toray Industries, Inc., 1-1, Sonoyama 1-chome, Otsu, Shiga 520-8558, Japan

[7] Department of Chemistry, The University of Tokyo, 7-3-1 Hongo, Bunkyo-ku, Tokyo 113-0033, Japan

[8] Center for Basic Research on Materials, National Institute for Materials Science, 1-1 Namiki, Tsukuba, Ibaraki 305-0044, Japan

ABSTRACT: Carbon fiber (CF) obtained by pyrolysis of polyacrylonitrile (PAN-CF) surpasses metals in properties suitable for diverse applications such as aircraft manufacture and power turbine blades. PAN-CF obtained by pyrolysis at 1200–1400 °C shows a remarkably high tensile strength of 7 GPa, much higher than pitch-based CF (pb-CF) consisting of piles of pure graphene networks. However, little information has been available on the atomistic structure of PAN-CF and on how it forms during pyrolysis. We pyrolyzed an acrylonitrile 9-mer in a carbon nanotube, monitored the course of the reaction using atomic-resolution electron microscopy and Raman spectroscopy, and found that this oligomer forms a thermally reactive wavy graphene-like network (WGN) at 1200–1400 °C during slow graphitization taking place between 900 °C and 1800 °C. Ptychographic microscopic analysis indicated that such material consists of 5-, 6-, and larger-membered rings; hence is not flat but wavy. The experimental data suggest that, during PAN-CF manufacturing, many layers of WGN hierarchically pile up to form a chemically and physically interdigitated noncrystalline phase that resists fracture and increases the tensile strength – the properties expected for high-entropy materials. pb-CF using nearly pure carbon starting material, on the other hand, forms a crystalline graphene network and is brittle.

INTRODUCTION

Pyrolysis of polyacrylonitrile (PAN, $(C_3H_3N)_n$) results in carbonization and weight loss to produce carbon fiber (CF) that surpasses metals in tensile strength, elastic modulus, strength-to-weight ratio, and chemical stability required by applications such as the manufacture of aircraft and power turbine blades (Figure 1a).[1,2,3,4] PAN-CF manufacturing is a complex process involving pyrolytic decomposition of PAN between 700 °C and 1800 °C, resulting in 32% weight loss.[5] A large part of nitrogen is lost between 1000 and 1200 °C,[6] and 99%-carbon PAN-CF is obtained at 1800 °C.[7] This complexity has created a long-standing puzzle on the nonlinear correlation between the tensile strength and the tensile modulus of PAN-CF (Figure 1b).[8] Of great practical and mechanistic interest is that the tensile strength of PAN-CF maximizes to 7 GPa at a process temperature of at 1200–1400 °C (intermediate temperature range, IT),[9] but, above 1800 °C, it drops to the level of pitch-based CF (pb-CF). pb-CF uses nearly pure carbon starting materials, graphitizes quickly at around 1000 °C, and forms a crystalline graphene network (GN).[10] Hence pb-CF is more brittle than PAN-CF and its materials properties are less controllable. These observations suggest that carbonizing PAN-CF (cPAN) at IT produces materials of chemical constitution and/or nano/microstructure different from GN.[11] Recent studies on bulk PAN-CF produced at IT have revealed the presence of multi-walled carbon nanotube (MWCNT) and curved graphene layers in the CF.[12] On the other hand, only well-ordered graphitic structures have been observed in pb-CF produced from carbon-rich pitch-based feedstock. Therefore, we considered that the non-planar GN contributes to the high mechanical properties of PAN-CF. Little atomistic information has, however been available on how PAN carbonizes in a graphitic environment and what kind of hierarchical structure it forms. We studied the temperature-dependent change of the structure of an acrylonitrile 9-mer (**AN9**) in the graphitic environment of a carbon nanotube (CNT) using atomic-resolution transmission electron microscopy (TEM) and scanning TEM (STEM) combined with bulk Raman analysis of CNTs containing the precursor. We report here the temperature-dependent formation of a series of morphologies of the carbonizing **AN9** (**cAN9**), including the formation of a nitrogen-containing carbonaceous structure below 900 °C, its

growth into a wavy graphene-like network (WGN) at IT, and the formation of a fully developed graphitic system at 1800 °C (Figure 1c). The WGN forming during pyrolysis of **cAN9** below 1600 °C consists of 5-, 6-, and larger-membered rings, hence, it is wavy, as indicated by atomistic ptychographic analysis of individual **cAN9**. The results obtained for **cAN9** suggest that the pyrolysis of PAN first produces small amorphous pieces of cPAN (Figure 1d left), then physically and chemically interdigitated noncrystalline WGNs (Figure 1d middle) when pyrolyzed at IT. WGNs eventually form crystalline graphite above 1800 °C, which may form intergranular voids hence causing fracture (Figure 1d right).[13] A recent report described a crystal structure of a model of the chemical connection between two GNs via 5- and 7-membered rings (Figure 1d middle).[14]

Single-molecule atomic-resolution time-resolved electron microscopy (SMART-EM) is a significant breakthrough in electron microscopy,[15] which allows us, with sufficient time and spatial resolution, to record the dynamics of molecular structures, monitor chemical reactions and their rates as a function of temperature, to observe intermediates, and, when integrated with other methods, to deduce the reaction pathways of individual molecules.[16,17,18,19] Atomic-resolution cinematography of several individual **cAN9**@CNT substances (which are, in fact, "molecules" like fullerene molecules) has shown its metamorphosis as it loses nitrogen and hydrogen between 700 °C and 1800 °C before the entire graphitization at 1800 °C (shown for a single "molecule" in Figure 2a). Most notably, **AN9** graphitizes only gradually during heating at 1000 °C and 1800 °C. Pyrolysis of **AN9** in CNT produces four morphologies: shapeless blobs (700–900 °C), footballs (1000–1100 °C), tubular half-graphitized **cAN9** (1200 °C), and fully graphitized tubes grown along the interior of the CNT (1800 °C, as supported by Raman spectroscopy). **cAN9** substances appearing below 1400 °C are thermally elastic, mobile, and chemically reactive substances.

They resemble in their shape the intermediates of the conversion of two C_{60} molecules (OT-11 and -14) into a short carbon nanotube C_{120} that takes place via a series of Stone–Wales rearrangements (SWR) of ring systems containing 5-, 6-, and 7-membered rings (Figure 2b).[20,21]

In contrast, a planar aromatic hydrocarbon (benzo[a]pyrene, **BaP**) used as a pitch model afforded a crystalline graphitic structure already at IT, while nitrogen-containing aromatics such as anthyridine and acridine produced wavy graphite structures like in the pyrolysis of **AN9**@CNT (Figure 1e). The difference between pb-CF and PAN-CF is reminiscent of the difference between crystalline metal and non-crystalline high entropy alloys, the former prone to grain boundary fracture.[22]

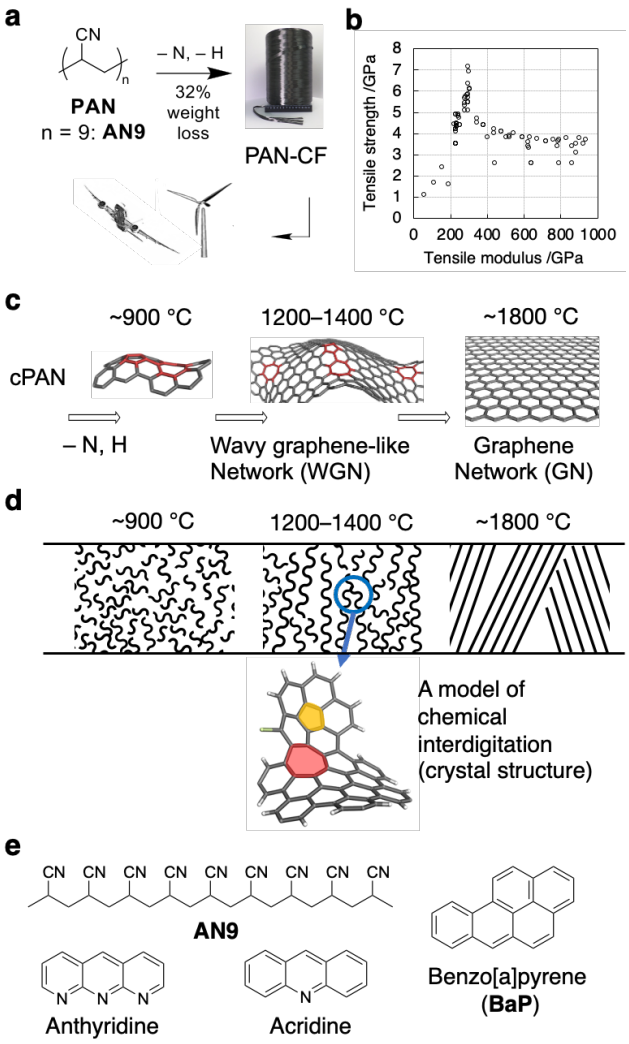

Figure 1. Carbon fiber (CF) formation by pyrolysis of polyacrylonitrile (PAN). (a) CF obtained via thermal conversion of PAN with the detachment of nitrogen and hydrogen and its applications. (b) Tensile strength/tensile modulus correlation for various PAN-CF taken from ref. 8. The CF with the highest tensile strength (7.2 GPa) is the PAN-CF processed at around 1200 °C, and the other data are PAN-CFs processed at other temperatures and pitch-based CFs. (c) The atomistic models of graphene-like intermediates of PAN-CF manufacturing between 800 °C and 1800 °C. (d) Illustration of sequential formation of PAN-CF as the processing temperature is raised: left, partially carbonized small amorphous pieces; middle, chemically and physically interdigitated WGNs; right, crystalline graphite and intergranular voids. A chemically synthesized model of a chemical interdigitation taken from ref. 14. (e) Chemical structures of precursor compounds used in this study.

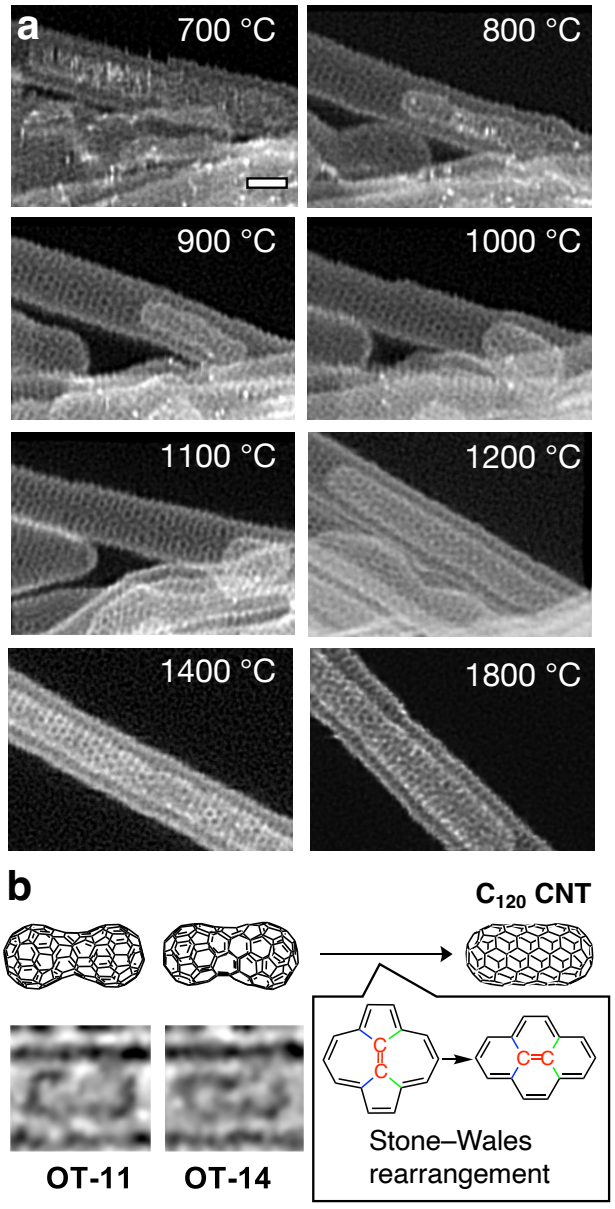

Figure 2. Atomic-resolution imaging of **cAN9** formed upon pyrolysis of **AN9**@CNT. (a) Sequential STEM images of an **AN9** molecule obtained by in situ heating between 700 °C and 1100 °C and another **AN9** molecule obtained by ex situ heating at 1200, 1400, and 1800 °C. Scale bar: 1 nm. (b) Images of two intermediates captured over 3.125 ms during C_{60} dimerization to form a short C_{120} CNT. The numbering was taken from ref. 20.

MATERIALS AND METHODS

Instrumentation. We used TEM and STEM in a complementary manner for atomic-resolution structural analysis of **cAN9**@CNT. In the TEM imaging, the high image contrast obtained because of the electron interference at the expense of reduced point resolution allows us to perform imaging of specimens made of light elements (such as **AN9**) with a low total electron dose (TED), that is, with a short exposure time per frame (cf Figure 2b). Thus, dynamic molecular processes can be tracked cinematographically with a temporal resolution of up to a submillisecond.[21,23] STEM, on the other hand, requires a TED higher than TEM by one order of magnitude because interference-enhancement of the image contrast does not operate here. The low scan rate (up to 24 frames per second, fps) is a limiting factor for the study of the dynamics of carbon-based molecules. For static and electron-stable specimens, STEM using a high TED produces clearer images than TEM. Ptychographic analysis available as 4D-STEM imaging of stable specimens is another asset of STEM.

Bright-field (BF)-STEM and high-angle annular dark-field (HAADF)-STEM observations were carried out on a JEOL JEM-ARM200F instrument equipped with a STEM aberration corrector (point resolution: 0.10 nm) at an acceleration voltage of 80 kV under 1×10^{-5} Pa in the specimen column. TEM observation was carried out on a JEOL JEM-ARM200F instrument equipped with a TEM aberration corrector (point resolution: 0.10 nm) and a complementary metal oxide semiconductor camera (Gatan OneView, 4,096 × 4,096 pixels, operated at binning 2 mode) at an acceleration voltage of 80 kV under 1×10^{-5} Pa in the specimen column. We used a spherical aberration (C_s) value between 1 and 3 µm. STEM observation for ptychographic analysis was carried out on a JEOL NEOARM equipped with a pixelated STEM detector (4DCanvas™, JEOL) with a fast direct electron charge-coupled device image sensor (pnCCD, PNDetector, maximum readout speed: 7,500 fps). Raman spectra were measured on an NRS-3200 spectrometer (JASCO Corporation) with an excitation wavelength of 785 nm.

Synthesis of AN9. We used an oligomer, **AN9**, as a model of PAN in the present study. Industrially used PAN is structurally impure because of comonomers and terminal groups derived from initiators and unsuitable for an atom-level study. First we examined a pentamer (4,6,8,10-tetracyanoundecanoic acid) and found it too mobile in a heated CNT for atomistic observation (Supporting Information, Figure S1). We also examined 1,9,10-anthyridine and acridine (Figure 1e) as less nitrogen-containing precursors and models of partially oxidized PAN formed by air oxidation at about 300 °C before carbonization at 1000–3000 °C.[24] The product obtained upon heating of anthyridine at 1000–1400 °C behaved similarly to that of **AN9** (Figure S2).

AN9 was synthesized in 11 steps (2% yield in total) by sequential elongation of the main chain in a three-step reaction of methacrylonitrile with *tert*-butyl cyanoacetate, alkylation with dibromomethane, and thermal decomposition (Scheme 1), following the method reported by Klaus.[25] The structure was determined using ^{1}H-NMR, ^{13}C-NMR, high-resolution mass spectrometry, and infrared spectroscopy (IR).

Scheme 1. Synthesis of **AN9**

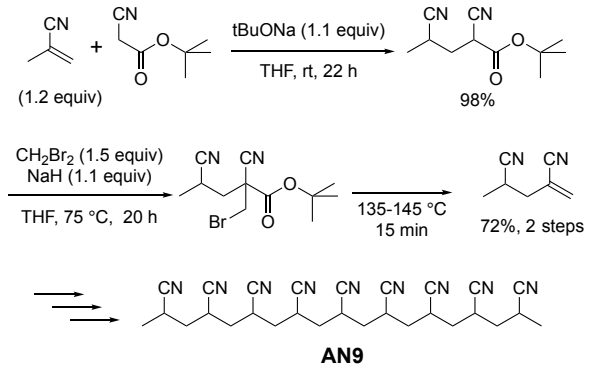

Preparation of AN9@CNT, BaP@CNT, anthyridine@CNT and acridine@CNT. To gain insights into atomistic features of

PAN carbonizing in the graphitic network developing during CF manufacturing, we used **AN9**@CNT as a model of cPAN in the carbon network. CNT is a conductive electron donor and protects organic molecules encapsulated therein from ionizing degradation (radiolysis) during TEM observation.[26] In this study, we encapsulated **AN9** in CNTs of 1.5–1.7 nm diameter. We monitored the process of graphitization of **AN9** by loss of nitrogen and hydrogen atoms with TEM by heating the specimen in a vacuum. CNTs of this diameter can avoid excessive thermal motions of **AN9** but are sufficiently large for the growth of a graphitic network to form a double-walled CNT (DWCNT, see below).[27]

Single-walled CNTs (Meijo Arc SO, produced by arc-discharge using Ni and Y catalysts, >90% purity, average diameter 1.5–1.7 nm determined based on the radial breathing modes (RBMs) in Raman spectra, Lot # 6601316) were purchased from Meijo Nano Carbon Co. Ltd. CNT powder was heated in the air in an oven gradually from 23 °C to 500 °C for 12 min, kept at 500 °C for 1 min, heated from 500 °C to 530 °C for 20 min and kept at 530 °C for 20 min to oxidatively remove the terminal caps of the CNTs. For encapsulation of **AN9**, the opened CNTs (1 mg) and **AN9** powder (1 mg) were sealed in a glass tube (Pyrex ϕ6 mm) under a pressure of 6.7×10^{-1} Pa and kept at 100 °C for 12 h (Figure 3). The resulting **AN9**-containing CNTs were separated from the remaining **AN9** powder. **AN9**@CNT thus obtained was a black solid (1 mg).

We used **BaP** as a model of a petroleum pitch which is a major precursor of pitch-based CFs, anthyridine as a model of a high nitrogen-content precursor, and acridine as a model of a low nitrogen-content precursor. For encapsulation of **BaP**, the opened CNTs (0.1 mg) and **BaP** powder (0.1 mg) were sealed in a glass tube (Pyrex ϕ6 mm) under a pressure of 6.7×10^{-1} Pa and kept at 200 °C for 12 h. The resulting **BaP**-containing CNTs were separated from the remaining **BaP** powder. **BaP**@CNT thus obtained was a black solid (0.1 mg). For the encapsulation of acridine or anthyridine, we prepared in the same procedure as **BaP**@CNT.

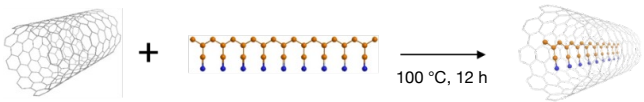

Figure 3. Schematic illustration of encapsulation of **AN9** into a CNT.

Carbonization of AN9@CNT, BaP@CNT, anthyridine@CNT and acridine@CNT at 700–1800 °C. Lin *et al*. reported that a long-range graphite structure begins to form at 700–900 °C, where PAN starts to carbonize with rapid loss of nitrogen and hydrogen atoms.[28] The images shown in Figure 2a indicated a substantial morphological change at 800–1000 °C and hence provided atomistic support to Lin's bulk analytical results. We, therefore, focused on a temperature range of 700–1800 °C to investigate the structural change of **AN9**. Experiments up to 1100 °C were performed in situ; that is, the specimen was heated in the TEM column and observed at regular time intervals by turning on the electron beam for several tens of seconds. Because of instrumental limitations, experiments above 1200 °C were performed ex situ; that is, the specimen was heated under a nitrogen atmosphere outside the TEM column, cooled, placed in the TEM column, and analyzed at room temperature.

In situ heating was performed on a microelectromechanical system (MEMS) device nanochip. After the target temperature was reached, the specimen was kept for 30–60 min to allow the structural changes to progress sufficiently at each temperature. The duration of electron irradiation on the sample for electron microscopy observation was limited to a maximum of several tens of seconds per measurement. We did not observe any morphological changes during the irradiation necessitated by the STEM and TEM imaging (i.e., the **cAN9**@CNT intermediates are resistant to irradiation).

For the ex situ experiments, we sealed **AN9**@CNT in a glass tube (Pyrex ϕ6 mm) under a pressure of 6.7×10^{-1} Pa and kept it at 600 °C for 1 h. In the experiments below 1100 °C, the precarbonized specimen was placed on a platinum pan under nitrogen and heated from room temperature to three temperatures (900, 1000, and 1100 °C) at a heating rate of 10 °C/min. In the experiments above 1100 °C, the precarbonized specimen was placed on a graphite furnace and kept at each temperature (1200, 1400, 1600, and 1800 °C) for 1 min under nitrogen. Each specimen was then analyzed by STEM or TEM. For the ex situ experiments of **BaP**@CNT, anthyridine@CNT and acridine@CNT, we prepared carbonized samples in the same procedure as **AN9**@CNT.

Preparation of samples for TEM and STEM experiments. We dispersed **cAN9**@CNT in toluene (0.05 mg/mL) in a vial in a bath sonicator for 1 h to soften it to secure good contact between the CNTs and the carbon surface of the grid (essential for temperature control).[27] For the ex situ experiments, a 10 μL solution of the dispersion was deposited on a microscopic grid or placed on a paper that absorbs excess toluene. The EM grid was dried in a vacuum (60 Pa) for 2 h to remove the solvent, then fixed on a TEM holder (JEOL EM-21130). For the in situ heating experiments, **AN9**@CNT in ethanol (ca 2 mg/mL) in a vial was sonicated in a bath sonicator for 1 h. A 10 μL solution of the dispersion was deposited on a MEMS chip (Wildfire, DENSsolutions) on a microelectrochemical system-based heating holder (Lightning, DENSsolutions). Finally, the in situ heating specimen was dried in air to remove the solvent. For **BaP**@CNT, we prepared an EM grid in the same procedure as **AN9**@CNT.

In situ observation of carbonization behavior of AN9@CNT at 700–1100 °C using scanning TEM. The images of in situ heating STEM at 700–1100 °C were captured at ×20,000,000 magnification, with a convergence semiangle of 24–27 mrad and a collection semiangle of 27–110 mrad. A comparison among the images obtained by STEM and TEM of the **cAN9** substances showed that the HAADF-STEM images provide richer structural information than the BF-STEM and TEM images (Figure S3). In the in situ experiments at 700–1100 °C, we continuously observed the translation, morphological changes, and chemical reactions of **cAN9** in the CNT (Figure 2a; see also Figure S4 for enlarged images). Below 700 °C, the image of **cAN9** was vaguely detected, reflecting that the amorphous nature of the **cAN9** still contained many nitrogen and hydrogen atoms.

Ex situ observation of carbonized AN9@CNT and BaP@CNT using TEM. We performed a statistical analysis of the structural features of **cAN9** and **cBaP** for specimens heated ex situ at various temperatures and analyzed them at room temperature by TEM. In addition, cinematographic imaging of the motions of individual carbonizing entities was performed to study their mobility in CNTs. We first surveyed many

cAN9 or **cBaP** entities encapsulated in CNTs as described above at ×400,000 magnification at a low electron dose rate (EDR, $<10^4$ e^- nm^{-2} s^{-1}). Upon finding suitable specimens, we set the EDR to ca 10^6 e^- nm^{-2} s^{-1} and magnification to the target value and started image capturing with 0.5 s exposure time. Image contrast was inverted when we obtained overfocused images.

Atomic-resolution STEM observation of carbonized AN9@CNT by ptychography. Because the atomic-resolution TEM imaging of structurally undefined molecules composed of light elements provides only low-contrast images, we performed ptychographic analysis, where one can correct lens aberrations of the optical system of the microscope used in the experiment.[29] Because the complete information on the phase of the electron probe is obtained, one can add an aberration correction function to the phase of the probe to create an aberration-free phase image, which made precise details of the structure visible. The method is effective for obtaining STEM images with a higher signal-to-noise ratio than the conventional annular dark-field (ADF) imaging method.[30,31] We simultaneously recorded a 4D dataset and an ADF-STEM image.

TEM image analysis. The images were collected as a .dm4 format file on Gatan DigitalMicrograph software and processed using ImageJ 1.50i software. The length of the **cAN9** and **cBaP** molecules was measured along the CNT major axis, and the width was measured perpendicular to the CNT major axis. The width was calculated as the average of two to five measurements for each molecule.

Raman Scattering. A unique feature of the SMART-EM method is that we can compare the average of the sum of the numerical information (e.g., reaction rate) for many individual molecules with the ensemble average for the bulk sample of the same molecule. Such comparison recently gave the first experimental proof of the quantum transition state theory for the interpretation of bulk kinetic data by the data obtained for individual reaction events by SMART-EM.[32] In this study, the statistical data on the behaviors of individual **AN9**@CNT molecules were obtained from the TEM/STEM observations. They were then compared with the Raman scattering data (ensemble average) obtained for the same bulk sample. We measured Raman spectra with an excitation wavelength of 785 nm. To avoid any side effects associated with heating, the laser power at the CNT surface was adjusted to be less than 3 mW using neutral density filters. The magnification of the objective lens was 100 times, giving a beam spot diameter of around 2 μm.

RESULTS AND DISCUSSION

The primary purpose of this study is to examine the chemical and physical properties of **cAN9** being pyrolyzed between 700 and 1800 °C with the ultimate goal of gaining insights into the origin of the extremely high tensile strength of PAN-CF processed at IT (Figure 1). To this end, we synthesized a well-defined model compound, **AN9**, put it into a CNT, and heated it in a vacuum at various temperatures for 30 to 60 min. The reaction was monitored by observing the **cAN9** using TEM or STEM (Figure 2a). The chemical structure of **cAN9** was further investigated by Raman analysis of bulk **cAN9**@CNT, which indicated that full graphitization of **cAN9** requires 1800 °C. The ptychographic STEM analysis provided direct evidence of an incomplete and wavy graphene-like structure at IT and a complete graphitic structure at 1800 °C. The nongraphitic intermediates forming below 1200 °C comprise 5-, 6-, and larger-membered rings (Figure 1c). They are mobile and chemically reactive to fuse, strongly suggesting their ability to form interdigitated noncrystalline networks in CF processed at IT (cf Figure 1d).

Structural Analysis of AN9@CNT by STEM. A BF-STEM image of the **AN9** molecule in CNTs before pyrolysis is shown in Figure 4, where we see a weak linear contrast with a linear distance between two ends of 1.78 nm and a curvilinear length along the molecule of about 2.26 nm. These data compare favorably with the calculated length of approximately 2.3 nm. We also found that **AN9** does not move for the STEM imaging time of 10 s due to CH/π and N/π interactions between **AN9** and the CNT inner wall. We thus confirmed that **AN9** was stably encapsulated in the CNT.

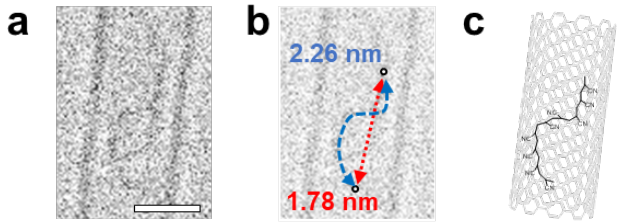

Figure 4. BF-STEM image of **AN9**@CNT. (a) A single **AN9** molecule in the CNT. (b) The same image as (a) with length annotations of the molecule. (c) Molecular model of the **AN9** molecule in the CNT. Scale bar: 1 nm.

In Situ Imaging of Thermal Transformation and Dynamic Motion of cAN9@CNT at 700–1100 °C. We next discuss the pyrolytic structural change of **AN9**@CNTs in Figure 2a. Upon heating to 700 °C, the linear outline of **AN9** disappeared in the HAADF-STEM image, and amorphous cloud-like objects appeared scattered along the CNT interior. At 700–800 °C, where nitrogen loss occurs, we see better defined but still amorphous ribbon-like objects, which we ascribe to nitrogen-rich polycyclic condensed aromatics—intermediates commonly assumed to be a precursor to CF.[24,33] They are longer than 4 nm in length, and shown to contain 5-, 6-, and larger-membered rings as shown by ptychography experiments discussed later (cf Figures 5 and 7). Bulk analysis of PAN pyrolysis at temperatures around 800 °C previously reported high nitrogen and hydrogen contents,[34] hence the lack of a well-developed graphitic structure.

At 900 °C, we find a dramatic change (Figure 2a): The **cAN9** molecule markedly shrank, and the high-contrast image indicates a higher atomic density in the depth direction due to the formation of a three-dimensional capsule-like structure formed from the amorphous one found at 800 °C. They look similar to the C_{60} dimerization intermediates (Figure 2b),[21] and must be rich in sp^2 carbon atoms as expected from the nitrogen loss observed in bulk experiments at 800–1000 °C.[24,33,35] Bulk experiments also indicated reduced intergraphitic distances (d_{002}) and conversion of sp^3 into sp^2 hybridization of the carbon atom.[36]

At 1000 °C, **cAN9** shrank further and changed its structure now resembling a football as seen in Figure 2a. Its outline is much smoother than we saw at 900 °C, and the carbon network has become more regular in structure as nitrogen and hydrogen loss progresses. The STEM image of Figure 2a between 800 °C and 1100 °C was taken at the same location, and we see translational motion upward. This result is consistent with the temperature conditions up to 1100 °C. Given that nitrogen loss at 900 °C

causes the formation of voids in CF, we surmise that cPAN forming during CF manufacture migrates in the void to find the most stable location. At 1100 °C, **cAN9** continues to migrate and becomes shorter. Bulk experiments indicate that the loss of nitrogen and hydrogen is almost complete in this temperature range,[24] and the microscopic observation fits very well with the bulk observation. The **cAN9** molecules at 1100–1200 °C migrated, reacted with each other, and grew in size (Figure 2a), suggesting that cPAN forming in CF manufacturing would similarly migrate, react, and create a complex network of to-be-graphene substances (i.e., WGN).

cAN9 pyrolyzed under 900 °C and the STEM images obtained by the ptychographic process are shown in Figure 5. In Figure 5a, we see an encapsulated **cAN9** apparently contains a substance other than 6-membered rings. To extract the structural information of this substance, we removed the contrast originating in the periodic CNT structure (Figure 5b) from Figure 5a and obtained the image of the encapsulated **cAN9** shown in Figure 5c. This image clearly indicates that the substance is not made exclusively of 6-membered rings, and resembles a typical Stone-Wales defect of graphene made of a heptagon flanked by two pentagons.[37] This structure accounts for the observed thermal plasticity of **cAN9**. Molecular dynamics simulations previously suggested that nitrogen loss from acrylonitrile precursors produces 5-membered rings. [38] In the STEM image of **cAN9**@CNT pyrolyzed at 1800 °C (i.e., DWCNT), we found neither 5- nor 7-membered ring (cf. Figure 7) in the image obtained by the same image processing.

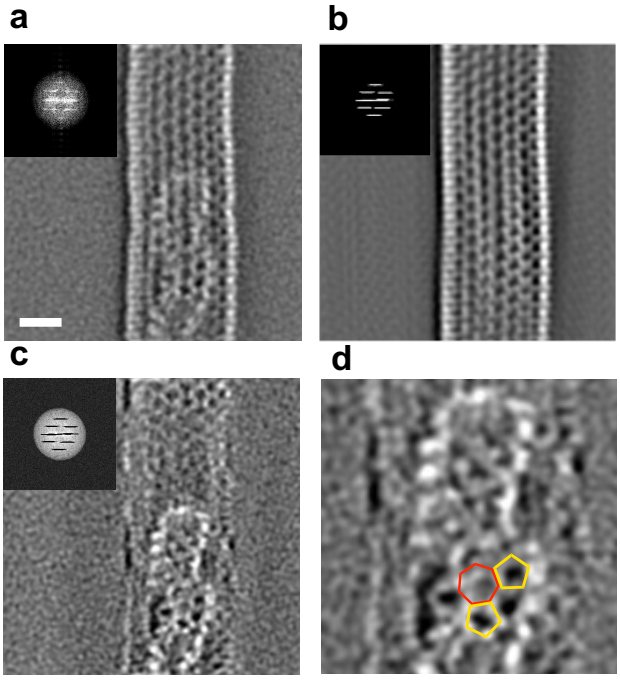

Figure 5. HAADF-STEM images of **AN9**@CNT treated at 900 °C reconstructed by ptychography. (a) STEM image of **AN9**@CNT. (b) Image of the CNT part extracted from (a) by FFT filtering. (c) A filtered image where the image contrast of CNT (b) was subtracted from (a). (d) A magnified image of (c) highlighting five- and seven-membered rings. Scale bar: 0.5 nm.

The mobility of **cAN9** in CNT was investigated further because the mobility of cPAN in pyrolyzing CF has never been suggested or discussed in the literature. To find the correlation between the structure and mobility of **cAN9**, we cinematographically followed, using TEM at room temperature, the dynamics of amorphous **cAN9** formed at 700 °C. The images in Figure 6 show the frequent translation of a 5-nm **cAN9** entity during 175 s, and we surmise that cPAN forming in void spaces of CF also moves frequently during pyrolysis. **cAN9** seen at higher temperatures, e.g., at 1100 °C (cf Figure 1d) also translates in the interior of the CNT, though far less frequently, and fuses to produce longer tubular objects, e.g., those seen at 1600 and 1800 °C (Figure 2a).

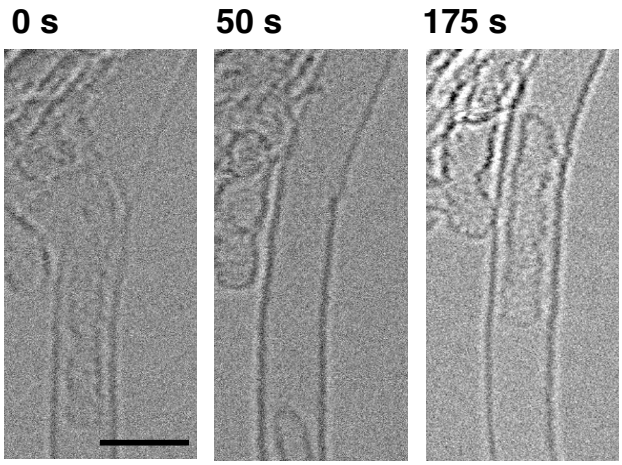

Figure 6. Sequential TEM images of **AN9**@CNT pyrolyzed at 700 °C showing high mobility of the **cAN9** molecule in the CNT. The timestamp denotes the time after starting the video recording. Scale bar: 2 nm.

Structural Analysis of cAN9@CNT at 1100–1800 °C. The reduced mobility of **cAN9** at temperatures higher than 1100 °C facilitated detailed structural analysis using ex situ TEM observation. We found an increase in the structural regularity and its growth along the CNT axis was more pronounced above 1400 °C where the carbon content exceeds 95% (measured for bulk PAN-CF).[7] The TEM images taken at 1100–1400 °C in Figure 7a, 7b and 7c show the change of the shape of a lumpy mass into a more regular structure. TEM images between 1600 °C and 1800 °C (Figure 7d,e), as well as STEM images (Figure 2a) show that the **cA9@CNT** forms a DWCNT, and has grown longer in the axial direction. The formation of complete DWCNT at 1800 °C was ascertained by the Raman analysis (see below).

Ptychographic reconstruction of **cAN9** pyrolyzed at 1800 °C in CNT is shown in Figure 7f–h. We used the same procedure as discussed in Figure 5 to remove the periodic structural component of the outer CNT (Figure 7g) from the original picture (Figure 7f). The inner CNT derived from **AN9** is shown in Figure 7h. Unlike **cAN9** in Figure 5c, we see a very regular graphitic structure in Figure 7h. Taken together with its linear outline, the data indicate that **cAN9** (i.e., inner CNT) produced at 1800 °C has defect-free graphene. The formation of a DWCNT observed here provides a plausible mechanism for the formation of the MWCNTs and the curved graphene layers isolated by disassembling the bulk PAN-CF sample by the use of ultrasound and supercritical liquid treatment.[12] The conversion of the structures in Figure 5 into those in Figure 7 resembles the SWR reaction in the transformation of OT-11 and OT-14 into a short CNT (Figure 2b).[21]

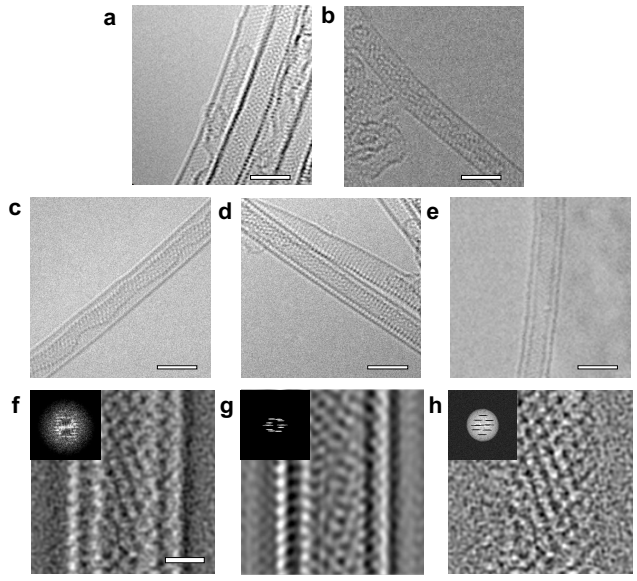

Figure 7. TEM and STEM images of **cAN9** obtained by ex situ thermal treatment of **AN9**@CNTs. (a–d) TEM images of **cAN9**@CNTs treated at (a) 1100 °C, (b) 1200 °C, (c) 1400 °C, and (d) 1600 °C. (e) STEM image of **cAN9**@CNTs treated at 1800 °C. (f) STEM image of **cAN9**@CNT treated at 1800 °C reconstructed by ptychography. (g) Image of the CNT part extracted from (f) by FFT filtering. (h) A filtered image where the image contrast of CNT (g) was subtracted from (f). Scale bars: 2 nm for a–e and 0.5 nm for f. See also Figure S5 for additional TEM/STEM images at each temperature.

Previous X-ray diffraction studies on bulk carbonization of PAN have shown that the average size of the crystallite (L_c, L_a) increases monotonically with increasing carbonization temperature.[36] We have seen in the present electron microscopic studies that individual **cAN9** entities shrank first as they lost nitrogen/hydrogen and grew larger by fusing. The SMART-EM method allows us to obtain statistical data from the individual **cAN9** entities, and compare them with the average data obtained for a bulk sample. We measured the sizes of **cAN9** entities observed by TEM for dozens of CNTs at different temperatures (Figure 8). The lengths measured in the direction axial to the CNT axis (length) are shown in Figure 8a, and those measured in the direction perpendicular to the axis (width) are shown in Figure 8b. The axial length of the CNTs did not change much at 900–1100 °C, averaging 4 nm, but grew significantly from 1400 °C onward, exceeding 10 nm and extending beyond the field of view. This observation is consistent with the individual STEM image shown in Figure 2a in that **cAN9** shrinks at 900–1000 °C whereas it grows longer at higher temperatures through the fusion of multiple **cAN9** entities.

The lengths measured at each temperature show a wide distribution because individual growth reaction events occurred stochastically—the norm for any chemical reaction at the molecular level.[27] The width of **cAN9** is distributed from 0.4 to 1.2 nm with an average value of 0.73 nm, and the average begins to increase at 1000 °C and finally converges to a distribution with an average value of 0.83 nm and individual values ranging from 0.8 to 0.9 nm at 1800 °C (Figure 8b). This indicates that the interaction between **cAN9** and CNTs is weak at low temperatures but becomes stronger, and the CNT inner wall acts as a template for SWR of WGN into flat graphene made solely of 6-membered rings.[7,39] We expect such a template effect to also operate in the process of pyrolysis of PAN to form the crystalline graphite CF region (cf Figure 1d).

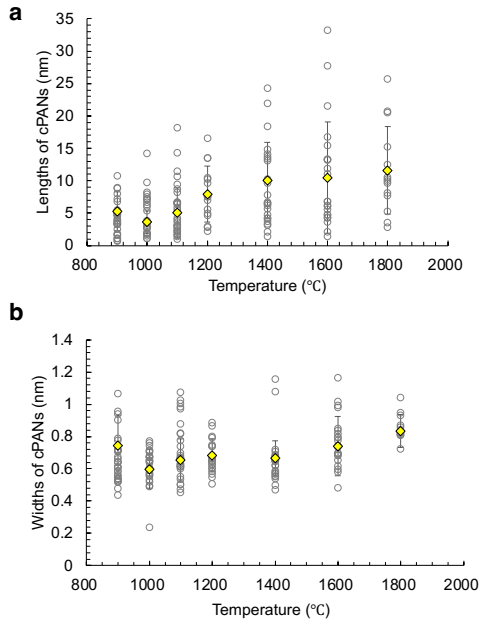

Figure 8. Statistical analysis of TEM images of **cAN9** formed in CNTs at different temperatures. (a) Length of **cAN9** measured along the axis of the CNT. (b) Width of **cAN9**. Circles denote data points and mean values are shown as rectangles.

Structural Analysis of carbonized benzo[a]pyrene@CNT at 1200–1800 °C. We studied by TEM the pyrolysis of **BaP@CNT** lacking nitrogen atoms as a model for pb-CF fabrication,[40] and found at 1200 °C an image of carbonized **BaP** (**cBaP**) resembling that of a graphene nanoribbon (GNR, Figure 9a).[41] In contrast, Figure 7b taken for **AN9@CNT** also at 1200 °C shows a structure lacking the sign of 6-membered ring graphitic structure. Heated at 1600 °C to 1800 °C, **cBaP**@CNT produced DWCNTs (Figure 9c, d). The comparison of the CNT axial lengths of the materials produced from **cAN9** and **cBaP** (Figure 9e) in the temperature range from 1200 to 1800 °C shows that **cBaP** gives substances of longer length (i.e., higher molecular weight).

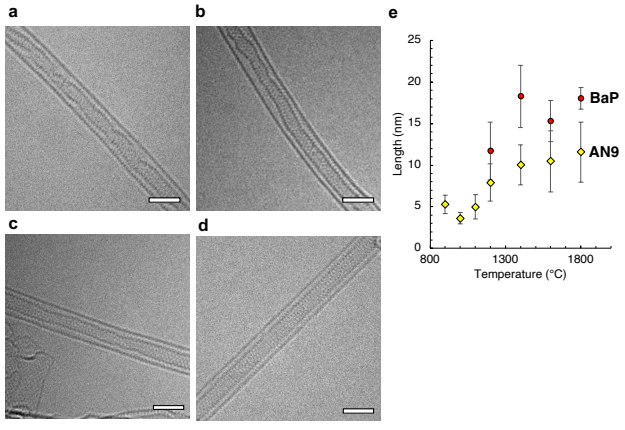

Figure 9. TEM image of cBaP@CNT. (a) 1200 °C, (b) 1400 °C, (c) 1600 °C, (d) 1800 °C, (e) Comparison of the length of **cAN9** and **cBaP** measured along the axis of the CNT.

Raman scattering of cAN9@CNT and BaP@CNT after thermal conversion. Raman spectra of bulk **cAN9**@CNT and **BaP**@CNT corroborate well with the results of the TEM analysis described above. First, we confirmed the formation of graphite network structure at long range by the RBM signal appearing around 100-400 cm^{-1}, and the growth of the G band due to a flat six-membered ring array by the signal at 1580 cm^{-1}. In the following paragraphs, we discuss the behavior of **AN9** and **BaP** at 1000–1800 °C, and the correlation between the nitrogen content in the precursors and the structure of the pyrolyzed product forming at 1400 °C.

In Figure 10a–c, we show a comparison of the Raman spectra between **AN9@CNT** and **BaP@CNT**. As shown in Figure 10a, The Raman spectra of the starting **AN9**@CNTs show two RBM signals at 155 cm^{-1} and 168 cm^{-1}, corresponding to diameters of 1.68 nm and 1.54 nm.[42] It was only at 1800 °C that a new signal at 271 cm^{-1} appeared indicative of a 0.9-nm diameter CNT, that is, a DWCNT. These data and the wavy outline of the encapsulated molecules seen by TEM indicate that the wall of **cAN9** formed below 1600 °C was not a flat graphitic network but was WGN (Figure 1c).

From **BaP**@CNT, DWCNTs are produced at lower temperatures than from **AN9**@CNTs, as judged by the appearance of the RBM signal (265 cm^{-1}), albeit small, already at 1600 °C. More strikingly, a 350 cm^{-1} signal originating in a radial-breathing-like mode (RBLM), [43] not found for **AN9**@CNT, began to appear at 1200 °C, reached a maximum at 1400 °C, and disappeared above 1600 °C, where the RBM peak of DWCNTs appeared. The 350 cm^{-1} signal is characteristic of planar six-membered-ring carbon structures such as GNR, and its appearance matches the crystalline structure detected by TEM at IT (see above).

In addition to the RBM region, the temperature-dependent variations in the G- and D-band regions also characterize the difference between **AN9**@CNT and **BaP**@CNT (Figure 10b). Pyrolysis of **BaP**@CNT at 1200–1400 °C results in the appearance of the G-band (1580 cm^{-1}) (Figure 10c). Since the outer CNT generates G^+-band at 1590 cm^{-1} and G^-–band at 1570 cm^{-1} (buried among other signals), we assign the 1580 cm^{-1} signal to the planar graphene structure. Using the G^+–band of the outer CNT as an internal standard, we quantified the intensity of the forming G-band (Figure 10d). **cAN9**@CNT showed almost no G-band at 1200-1400 °C (yellow line), whereas **cBaP**@CNT showed the G-band (blue line) which disappeared at 1600 °C. In response to this disappearance, the RBM signal of 265 cm^{-1} appeared, i.e., the production of DWCNT. Finally, for both **AN9**@CNT and **BaP**@CNT, the G-band (1580 cm^{-1}) and G^+-bands disappeared at 1800 °C and G-band of DWCNT appeared at 1585 cm^{-1} (Figure 10c). For the D-band region, the intensity of a new D-band (1280 cm^{-1}), which appeared at a different position from the outer CNT-derived D band (1300 cm^{-1}), is also stronger for **cBaP**@CNT than in **cAN9**@CNT. It is consistent with the spectral change in the RBM region where the conversion **cBaP** to the GNR-like substance occurs at IT (Figure 10b).

In summary, **AN9@CNT** below 1400 °C produces WGN, at 1600 °C produces a planar substance, and finally form DWCNT at 1800 °C. On the other hand, **BaP@CNT** forms planar GNR already at 1200 °C, and starts to form DWCNT at 1600 °C completing at 1800 °C.

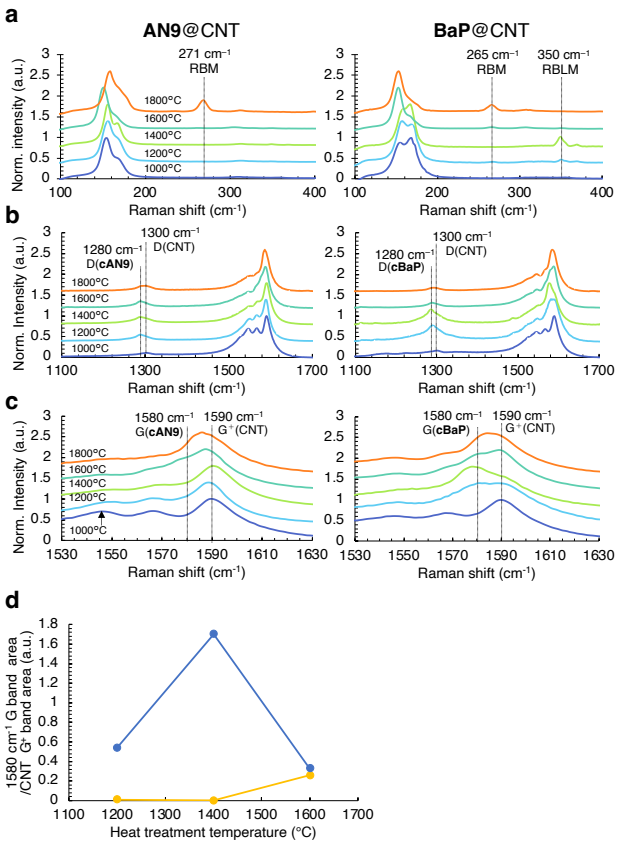

Figure 10. Raman spectra of **AN9**@CNT and **BaP**@CNT treated at 1000 to 1800 °C. (a) RBM and RBLM region. (b) G- and D-band region. (c) G-band region. (d) Comparison of the G-band intensity normalized by G^+-band at different temperatures.

Raman scattering of carbonized N-containing PAH precursors@CNT after thermal conversion. Next, we compared the thermal behavior of CF precursors with nitrogen content varying from 0% to 32.14% at 1400 °C. We focused on the peak intensity of the G-band (1580 cm^{-1}) As is seen in Figure 11a and summarized in Figure 11b, we found the increase in the nitrogen content causes the decrease of the G-band, indicating that nitrogen suppresses the formation of the planar graphene structure. Thus, **BaP** consisting only of carbon and hydrogen atoms gives a strong G-band, while acridine with a nitrogen content of 7.69% gives only a shoulder peak at 1580 cm^{-1}. Anthyridine with 27.28% nitrogen content and **AN9** with 32.14% nitrogen content show no G-band at all at 1580 cm^{-1}. We noted however that all four precursors gave DWCNTs when heated to 1800 °C where nitrogen atoms are entirely lost (cf. Figure 10a, b).

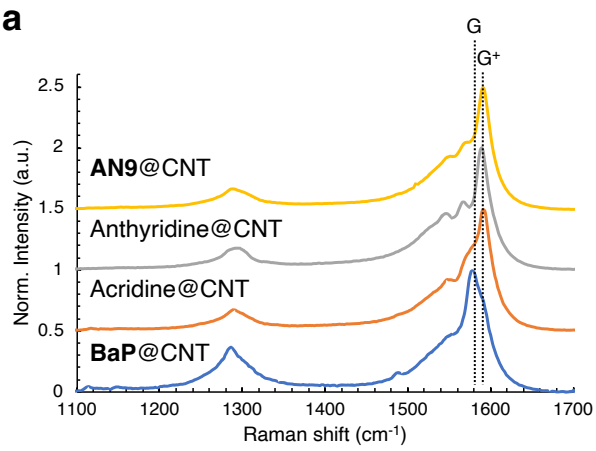

b

Compound	Formula	N/C (%)	G/G$^+$
BaP@CNT	$C_{20}H_{12}$	0	1.70
Acrydine@CNT	$C_{13}H_9N$	7.69	0.12
Anthyridine@CNT	$C_{11}H_7N_3$	27.28	0
AN9@CNT	$C_{28}H_{31}N_9$	32.14	0

Figure 11. Raman spectra of nitrogen-containing precursors in CNT upon pyrolysis at 1400 °C. (a) G-band and D-band spectra of CNTs encapsulated with **AN9**, anthyridine, acridine, and **BaP**. (b) Correlation between the nitrogen content of the precursor and G/G$^+$-band ratio.

CONCLUSION

Industrially produced PAN-CF has a tensile strength of 7 GPa,[44,45] which may even reach 19–23 GPa.[46,47] However, the elastic modulus of 600 GPa remains rather unimpressive, compared with the data reported for pb-CF, which has achieved 965 GPa, comparable to a CNT.[48] At the same time, the maximum tensile strength is only 4 GPa.[8] Achieving both high tensile strength and high modulus for PAN-CF has been a long-standing challenge in the materials community. However, our effort to improve the tensile strength of PAN-CF has been hampered by the lack of understanding of the origin of the high tensile strength, in particular, the reason why the tensile strength maximizes at IT.

A consensus has been that the imbalance between tensile strength and elastic modulus of PAN-based CF is due to its three-component composition, consisting of a highly periodic graphitic portion, an aperiodic portion with an unknown structure, and voids.[49,50] The least known has been the chemical structure of the aperiodic structure and its role in the mechanical properties—a bottleneck of the PAN-CF research. The present study suggests that both the imbalance and the temperature dependence of the mechanical properties are closely related to the formation of WGN upon pyrolysis at IT (Figure 1d). Such structure will resist fracture because of high entropy that suppresses further entropy increase (e.g., fracturing).

The comparison of the thermal behavior of **BaP@CNT** and **AN9@CNT** shows that the former forms a planar graphene structure at IT before forming DWCNT at 1600 °C, whereas the latter forms a 5-, 6-, and 7-membered WGN as a semi-stable structure before forming DWCNT at 1800 °C. As formed in the bulk CF, the disordered WGN structure should resist crystallization and hence enhance the mechanical properties from an entropic point of view, while crystalline graphite structure would prone to grain boundary fracture. This difference between pb-CF and PAN-CF is reminiscent of the difference between crystalline metal and non-crystalline high entropy alloys, the former prone to grain boundary fracture.[22]

We have compared in this study the bulk data, the properties of individual molecules, and the ensemble average data determined using TEM/STEM observations and suggest a scenario for pyrolyzed PAN to achieve high tensile strength at IT. Before the rapid nitrogen decomposition around 900 °C, cPAN is amorphous and thermoelastic so that it can move among voids formed by nitrogen/hydrogen loss (as large as 32% mass loss). The cPAN produced at 900 °C consists of 5-, 6-, and 7-membered rings, and further nitrogen loss occurs around 1100 to 1200 °C, where the cPAN forms aperiodic stacks of WGN. Templated promotion of the growth of graphitic layers has been suggested previously by the isolation of MWCNTs and curved multigraphene layers.[12]

The data have shown that the high nitrogen content of PAN plays a crucial role in the production of CF with high tensile strength, because the nitrogen loss at IT is critical in that it produces the WGN that shows thermoelectricity due to SWR. The presence of WGN may destabilize PAN-CF due to a decrease in enthalpy but stabilize it due increase in entropy so that the CF resists further increase of entry by fracture. The observed conversion of wavy graphene to order graphene resembles the 2-D and 3-D crystal nucleation/growth processes recently observed by the SMART-EM method.[18,51] The situation differs for pb-CF, where graphitization and crystallization occur nearly at once at around 1000 °C to form a full-fledged graphite structure, resulting in less hierarchical mesostructure and thus leaving little chance for structure control. Finally, we note in passing the renewed interest in the ubiquity of carbon and carbon-based materials these days for nonscientific but nontrivial reasons,[52,53] such as geographically uneven distribution of metal resources and the decreasing supply of even common elements, for example, high-grade iron ore.

ASSOCIATED CONTENT

Supporting Information

The Supporting Information is available free of charge on the ACS Publications website.

Additional materials and methods and supporting figures (PDF)

AUTHOR INFORMATION

Corresponding Authors

fumihiko.tanaka.w8@mail.toray
harano.koji@nims.go.jp
nakamura@chem.s.u-tokyo.ac.jp

ACKNOWLEDGMENT

We thank Prof. Kazu Suenaga (Osaka Univ.) for helpful discussion of TEM observations of AN5. This research is supported by JSPS KAKENHI (JP19H05459, JP21H01758, JP22K14704, and JP23H04874).

REFERENCES

[1] Morgan, P., Carbon fibers and their composites. CRC press: 2005.
[2] Frank, E.; Hermanutz, F.; Buchmeiser, M. R., Carbon Fibers: Precursors, Manufacturing, and Properties. *Macromol. Mater. Eng.* **2012,** *297*, 493–501.
[3] Morita, K.; Murata, Y.; Ishitani, A.; Murayama, K.; Ono, T.; Nakajima, A., Characterization of commercially available PAN (polyacrylonitrile)-based carbon fibers. *Pure Appl. Chem.* **1986,** *58*, 455–468.
[4] Park, S.-J., *Carbon fibers.* Springer: **2015**; Vol. 210.
[5] Dang, W.; Liu, J.; Wang, X.; Yan, K.; Zhang, A.; Yang, J.; Chen, L.; Liang, J., Structural transformation of polyacrylonitrile (PAN) fibers during rapid thermal pretreatment in nitrogen atmosphere. *Polymers* **2020,** *12*, 63.
[6] Fitzer, E. Pan-Based Carbon Fibers—Present State and Trend of the Technology from the Viewpoint of Possibilities and Limits to Influence and to Control the Fiber Properties by the Process Parameters. *Carbon* **1989**, *27*, 621–645.
[7] Xiao, P.; Gong, Y.; Li, D.; Li, Z., In-situ SAXS study on pore structure change of PAN-based carbon fiber during graphitization. *Microporous and Mesoporous Materials* **2021,** *323*, 111201.
[8] Tanaka, F.; Okabe, T., Historical review of processing, microstructures, and mechanical properties of PAN-based carbon fibers. In *Comprehensive composite materials II*, Elsevier: 2017; pp 66–85.
[9] Cooper, G. A.; Mayer, R. M., Strength of carbon fibres. *J. Mater. Sci.* **1971,** *6*, 60-67.
[10] Matsumoto, T., Mesophase pitch and its carbon-fibers. *Pure Appl. Chem.* **1985,** *57*, 1553–1562.
[11] Qin, X.; Lu, Y.; Xiao, H.; Wen, Y.; Yu, T., A comparison of the effect of graphitization on microstructures and properties of polyacrylonitrile and mesophase pitch-based carbon fibers. *Carbon* **2012,** *50*, 4459–4469.
[12] Ono, K.; Tomai, T.; Ishii, T.; Kurushima, K.; Inamoto, S.; Rutz, B. H.; Tanaka, F., Direct evidence for highly developed graphene in PAN-based carbon fibers. *Carbon Trends* **2021,** *5*, 100136.
[13] Li, D.; Lu, C.; Wang, L.; Du, S.; Yang, Y., A reconsideration of the relationship between structural features and mechanical properties of carbon fibers. *Materials Science and Engineering: A* **2017,** *685*, 65–70.
[14] Fernández-García, J.; Evans, P. J.; Rivero, S. J.; Fernández, I.; García-Fresnadillo, D.; Perles, J.; Casado, J.; Martín, N. π-Extended Corannulene-Based Nanographenes: Selective Formation of Negative Curvature, *J. Am. Chem. Soc.* **2018**, *140*, 17188–17196.
[15] Keinan, E. A Scientist and a Musician. *AsiaChem.* **2021**, *2*, 96–103.
[16] Koshino, M.; Tanaka, T.; Solin, N.; Suenaga, K.; Isobe, H.; Nakamura, E. Imaging of Single Organic Molecules in Motion. *Science* **2007**, *316*, 853.
[17] Nakamura, E. Atomic-Resolution Transmission Electron Microscopic Movies for Study of Organic Molecules, Assemblies, and Reactions: The First 10 Years of Development. *Acc. Chem. Res.* **2017**, *50*, 1281–1292.
[18] Nakamuro, T.; Sakakibara, M.; Nada, H.; Harano, K.; Nakamura, E. Capturing the Moment of Emergence of Crystal Nucleus from Disorder. *J. Am. Chem. Soc.* **2021**, *143*, 1763–1767.
[19] Harano, K. Self-Assembly Mechanism in Nucleation Processes of Molecular Crystalline Materials. *Bull. Chem. Soc. Jpn.* **2021**, *94*, 463–472.
[20] Han, S.; Yoon, M.; Berber, S.; Park, N.; Ōsawa, E.; Ihm, J.; Tománek, D. Microscopic Mechanism of Fullerene Fusion. *Phys. Rev. B.* **2004**, *70*, 113402.
[21] Shimizu, T.; Lungerich, D.; Harano, K.; Nakamura, E. Time-Resolved Imaging of Stochastic Cascade Reactions over a Submillisecond to Second Time Range at the Angstrom Level. *J. Am. Chem. Soc.* **2022**, *144*, 9797–9805.
[22] George, E. P.; Raabe, D.; Ritchie, R. O. High-Entropy Alloys. *Nat. Rev. Mater.* **2019**, *4*, 515–534.
[23] Shimizu, T.; Lungerich, D.; Stuckner, J.; Murayama, M.; Harano, K.; Nakamura, E. Real-Time Video Imaging of Mechanical Motions of a Single Molecular Shuttle with Sub-Millisecond Sub-Angstrom Precision. *Bull. Chem. Soc. Jpn.* **2020**, *93*, 1079–1085.
[24] Fitzer, E.; Hevire, M., Carbon Fibre Manufacture and Surface Treatment in" Fibre Reinforcement for Composite Materials", AR Bunsell Ed. Elsevier Amsterdam: 1988.
[25] Klaus, R.; Nino, H.; Andreas, F. Detailed examination of nitrile vibrations relevant for understanding the behavior of thermally treated polyacrylonitrile. *J. Polym. Sci.* **2017**, *134*, 44936.
[26] Liu, D.; Kowashi, S.; Nakamuro, T.; Lungerich, D.; Yamanouchi, K.; Harano, K.; Nakamura, E. Ionization and Electron Excitation of C_{60} in a Carbon Nanotube: A Variable Temperature/Voltage Transmission Electron Microscopic Study. *Proc. Natl. Acad. Sci. U.S.A.* **2022**, *119*, e2200290119.
[27] Okada, S.; Kowashi, S.; Schweighauser, L.; Yamanouchi, K.; Harano, K.; Nakamura, E., Direct Microscopic Analysis of Individual C_{60} Dimerization Events: Kinetics and Mechanisms. *J. Am. Chem. Soc.* **2017**, *139*, 18281–18287.
[28] Lin, X.; Wang, C.; Yu, M.; Lin, Z.; Liu, Y. Study on the relatioships of mechanical performance with the short-range and long-range structure of 500-900 carbonized fiber. *Journal of Industrial Textiles* **2015**, *45*, 33–47.
[29] Yang, H.; Rutte, R. N.; Jones, L.; Simson, M.; Sagawa, R.; Ryll, H.; Huth, M.; Pennycook, T. J.; Green, M. K. L.; Soltau, H.; Kondo, Y.; Davis, B. G.; Nellist, P. D. Simultaneous atomic-resolution electron ptychography and Z-contrast imaging of light and heavy elements in complex nanotrructures. *Nat. Commun.* **2016**, *7*, 12532.
[30] Nellist, P. D.; McCallum, B. C.; Rodenburg, J. M. Resolution beyond the 'information limit' in transmission electron microscopy. *Nature* **1995**, *374*, 630–632.
[31] Pennycook, T. J.; Lupini, A. R.; Yang, H.; Murfitt, M. F.; Jones, L.; Nellist, P. D. Efficient phase contrast imaging in STEM using a pixelated detector. Part 1: experimental demonstration at atomic resolution. *Ultramicroscopy* **2015**, *151*, 160–167.
[32] Nakamura, E.; Harano, K. Chemical Kinetics Study through Observation of Individual Reaction Events with Atomic-Resolution Electron Microscopy. *Proc. Jpn. Acad. Ser. B* **2018**, *94*, 428–440.
[33] Guigon, M.; Oberlin, A. Heat-treatment of high tensile strength PAN-based carbon fibers: Microstructure, structure and mechanical properties. *Comp. Sci. Tech.* **1986**, *27*, 1–23.
[34] Morita, K.-i.; Miyachi, H.; Hiramatsu, T., Stabilization of acrylic fibers by sulfur atoms mechanism of stabilization. *Carbon* **1981,** *19*, 11–18.
[35] Lee, J. -E.; Choi, J.; Lee, D. J.; Lee, S.; Chae, H. G. Radial microstructure development of polyacrylonitrile (PAN)-based carbon fibers. *Carbon* **2002**, *191*, 515–524.
[36] Takaku, A.; Shioya, M., X-ray measurements and the structure of polyacrylonitrile-and pitch-based carbon-fibers. *J. Mater. Sci.* **1990,** *25*, 4873–4879.
[37] Hashimoto, A.; Suenaga, K.; Gloter, A.; Urita, K.; Iijima, S. Direct Evidence for Atomic Defects in Graphene Layers. *Nature* **2004**, *430*, 870–873.
[38] Saha, B.; Schatz, G. C., Carbonization in polyacrylonitrile (PAN) based carbon fibers studied by ReaxFF molecular dynamics simulations. *J. Phys. Chem. B* **2012,** *116*, 4684–4692.
[39] Saha, B.; Furmanchuk, A. o.; Dzenis, Y.; Schatz, G. C., Multi-step mechanism of carbonization in templated polyacrylonitrile derived fibers: ReaxFF model uncovers origins of graphite alignment. *Carbon* **2015,** *94*, 694–704.
[40] Zieliński, J.; Osowiecka, B.; Liszyńska, B.; Ciesińska, W.; Polaczek, J.; Kubica, K. Benzo[a]Pyrene in Coal Tar Pitch: Chemical Conversion in Situ by Alkylation. *Fuel* **1996**, *75*, 1543–1548.
[41] Talyzin, A. V.; Anoshkin, I. V.; Krasheninnikov, A. V.; Nieminen, R. M.; Nasibulin, A. G.; Jiang, H.; Kauppinen, E. I. Synthesis of Graphene Nanoribbons Encapsulated in Single-Walled Carbon Nanotubes. *Nano Lett.* **2011**, *11*, 4352–4356.
[42] Dresselhaus, M. S.; Dresselhaus, G.; Saito, R.; Jorio, A., Raman spectroscopy of carbon nanotubes. *Phys. Rep.* **2005**, *409*, 47–99.
[43] Overbeck, J.; Barin, G. B.; Daniels, C.; Perrin, M. L.; Braun, O.; Sun, Q.; Darawish, R.; Luca, M. D.; Wang, X.-Y.; Dumslaff, T.; Narita,

A.; Müllen, K.; Ruffieux, P.; Meunier, V.; Fasel, R.; Calame, M. A Universal Length-Dependent Vibrational Mode in Graphene Nanoribbons. *ACS Nano* **2019**, *13*, 13083–13091.

[44] Yamane, S.; Hiramatsu, T.; Higuchi, T., Torayca" T 1000 Ultra High Strength Carbon Fiber and Its Composite Properties. *Advan. Mater. Tech.'87* **1987**, 928–937.

[45] Hiramatsu, T.; Nishimura, T., Recent technological progress of PAN-based carbon fibre. *Mater. Design* **1989,** *10*, 93–100.

[46] Ito, A.; Okamoto, S., Using molecular dynamics to assess mechanical properties of PAN-based carbon fibers comprising imperfect crystals with amorphous structures. *International Journal of Mechanical and Mechatronics Engineering* **2013,** *7*, 1840–1845.

[47] Penev, E. S.; Artyukhov, V. I.; Yakobson, B. I., Basic structural units in carbon fibers: Atomistic models and tensile behavior. *Carbon* **2015,** *85*, 72–78.

[48] Minus, M. L.; Kumar, S., The processing, properties, and structure of carbon fibers. *JOM* **2005,** 57, 52–58.

[49] Tanaka, F.; Okabe, T.; Okuda, H.; Ise, M.; Kinloch, I. A.; Mori, T.; Young, R. J., The effect of nanostructure upon the deformation micromechanics of carbon fibres. *Carbon* **2013**, *52*, 372–378.

[50] Tane, M.; Okuda, H.; Tanaka, F., Nanocomposite microstructures dominating anisotropic elastic modulus in carbon fibers. *Acta Materialia* **2019**, *166*, 75–84.

[51] Sakakibara, M.; Nada, H.; Nakamuro, T.; Nakamura, E. Cinematographic Recording of a Metastable Floating Island in Two- and Three-Dimensional Crystal Growth. *ACS Cent. Sci.* **2022**, *8*, 1704–1710.

[52] López-Salas, N.; Antonietti, M. Carbonaceous Materials: The Beauty of Simplicity. *Bull. Chem. Soc. Jpn.* **2021**, *94*, 2822–2828.

[53] Nakamura, E.; Sato, K. Managing the Scarcity of Chemical Elements. *Nat. Mater.* **2011**, *10*, 158–161.

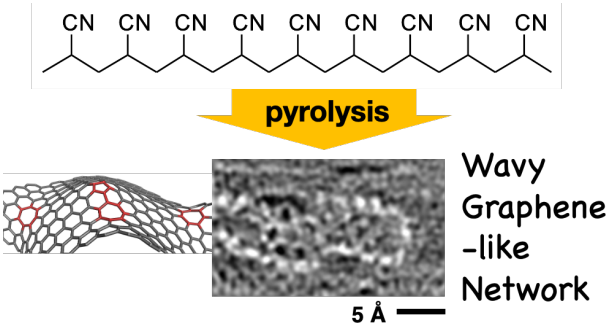
CN CN CN CN CN CN CN CN CN
pyrolysis
Wavy
Graphene
-like
Network
5 Å